Beam transit effects in single molecule coherent diffraction

J. M. Gibson
Advanced Photon Source, Argonne National Laboratory, 9700 S. Cass Avenue, Argonne, Illinois 60439-4856, USA

M. M. J. Treacy
Department of Physics, Arizona State University, P.O. Box 871504, Tempe, Arizona 85287-1504, USA
(Received 16 August 2008; revised manuscript received 1 October 2008; published 1 December 2008)

We explore how phase and amplitude gradients, which are almost inevitable in a coherent illumination probe, affect the atomic reconstruction of an isolated molecule based on diffraction intensities. By modeling the probe as a defocused Gaussian source, we show that structural distortion can be introduced in the reconstructed object if plane-wave illumination is assumed in the diffraction phase-retrieval algorithm. For the plane-wave approximation, we conclude that the standard deviation σ_d describing the source width should be such that $\sigma_d \sim 10R_c$, where R_c is the nominal radius of the molecule. In a pulsed source, where diffraction data are obtained when the moving molecule is at an instantaneous location within the illumination window, the effects of wave front curvature can be reduced by defocusing the illumination. This improvement comes at the expense of a weaker diffraction signal. For the three-dimensional reconstruction of a molecule, diffraction patterns from many different orientations of identical molecules are required. Since phase-retrieval methods are inherently solving for the probe plus the molecule, irreproducibility of wave front curvature or molecule location within the probe will introduce additional degrees of freedom to the structure solution problem.

DOI: 10.1103/PhysRevB.78.245401 PACS number(s): 61.05.Np, 61.05.cf

I. INTRODUCTION

Recent experiments and theory indicate that it will soon be possible to reconstruct the three-dimensional structure of protein molecules by obtaining serial diffraction data as a beam of isolated similar molecules traverses a high-intensity x-ray or electron beam.[1–7] This is an exciting development in diffraction physics, made necessary by the fact that a high proportion of proteins does not crystallize and thus their structures cannot be solved by standard crystallographic methods. Low-dose cryotransmission electron microscopy has been applied successfully to the problem by obtaining many images of identical objects on thin supports and tomographically reconstructing the three-dimensional structure. This however, is a time-consuming exercise with limited resolution.[8] The alternative diffraction approaches, both electron and x ray, are not without their difficulties. Coherent high-brightness sources are essential to such experiments, where the diffracted signal is inherently weak. High brightness synchrotron and free-electron laser sources, as well as x-ray lenses for focusing the illumination, are being developed that will meet this need. The technology to create stable droplet beams containing isolated particles has been demonstrated,[2,9] and there has been a recent proliferation of phase-retrieval techniques for inverting diffraction data.[10–17]

Successful phase retrieval at high spatial resolution requires knowledge of the illumination wave function. Plane-wave illumination conditions can simplify certain aspects of the phase-retrieval algorithm by eliminating the need to solve also for the absolute location of the molecule within the probe. In fact, for a plane wave, the absolute location of the molecule cannot be determined if the diffraction phases are not measured directly—the diffraction intensities from different locations being indistinguishable. It is known that phase and amplitude gradients in the illumination have an important effect on the interference between scattered waves and all phase-retrieval methods require knowledge of the illumination wave front at the sample.[10–13] Further, to generate sufficient illumination intensity at the object in order to increase the diffracted signal, some focusing of the illumination is necessary. It has been pointed out that wave front curvature is useful for resolving phase ambiguities in object reconstructions, provided the wave front is known.[13] Methods for object reconstruction by phase retrieval necessarily solve for the whole scattering system—the probe plus the molecule. The location of the molecule within the probe is an inherent component of the diffraction data.

In this paper, we explore the effects of phase and amplitude gradients on the diffraction from isolated molecules at various locations within a model probe of Gaussian intensity profile. We show that even small amounts of wave front curvature and amplitude gradients can degrade significantly the object reconstruction when plane-wave illumination is assumed. We conclude that for an illumination with intensity profile standard deviation σ_d, the condition $\sigma_d \sim 10R_c$ is about optimum for a molecule of radius R_c. Problems occur in reconstruction if the object moves during exposure or if the data are ensemble-averaged encompassing a variety of relative positions before reconstruction. We set limits on the extent of focusing that maintain the validity of the plane-wave approximation.

II. KINEMATICAL DIFFRACTION MODEL

In this section, we develop an analytical model for the scattering by an object (i.e., a molecule) that is irradiated by a focused electron probe. Our treatment is easily modified for x-ray scattering by incorporating the appropriate polarization factor for the scattering. The object is not necessarily centered on the probe and can even move across the probe to produce a time-averaged diffraction pattern. The probe is

modeled with a Gaussian intensity profile, a form that allows analytical expressions to be obtained. Our general conclusions are expected to hold for other probe profiles, such as those generated near pinholes or near the foci of zone plates. We ignore internal motions of the molecule, such as rotations and beam damage during exposure, since their deleterious effects on structure determination are already well understood.

The specimen is treated as a moving finite assembly of N atoms. At time t, atom j is at position $\boldsymbol{r}'_j(t)$. It is convenient to represent the trajectory of each atom as comprising two separate motions: the motion of the assembly's center of mass $\boldsymbol{R}(t)$ plus the motion with respect to that center of mass $\boldsymbol{r}_j(t)$. Thus, we write

$$\boldsymbol{r}'_j(t) \equiv \boldsymbol{R}(t) + \boldsymbol{r}_j(t). \tag{1}$$

The location of the center of mass is

$$\boldsymbol{R}(t) = \frac{1}{N}\sum_{j=1}^{N} \boldsymbol{r}'_j(t). \tag{2}$$

If the assembly is rigid and not rotating, $\boldsymbol{r}_j$ is constant and the time-dependent part of the trajectory is contained entirely in $\boldsymbol{R}(t)$. During a scattering experiment, momentum and energy are necessarily imparted to the assembly, potentially causing changes to both $\boldsymbol{R}(t)$ and $\boldsymbol{r}_j(t)$. This is especially true for experiments of the "diffract-and-destroy" variety where short high energy x-ray pulses are scattered from the object.[4,7] In all scattering experiments, we measure a time-averaged scattering profile. If the pulse duration is significantly shorter than the inertial response time of the individual atoms within the destroyed molecule, the diffraction data is then mostly from the initial pristine structural state.[18] In such experiments it is assumed that all of the $\boldsymbol{r}_j$ are essentially constant during the exposure and that atomic ionization has not significantly altered the scattering properties of the molecule.

First, we consider the sample to be illuminated by plane-wave radiation of wavelength λ and wave vector amplitude $\kappa = 2\pi/\lambda$, with vector component $\boldsymbol{k}$ relative to the optic axis (Fig. 1). The radiation is scattered into an outgoing plane-wave vector $\boldsymbol{q}$ relative to the optic axis. The amplitude of the scattered wave far from the sample, in the Fraunhofer limit expected in coherent diffraction experiments, is[19–21]

$$\phi_j(\boldsymbol{r}'', \boldsymbol{r}'_j, \boldsymbol{k}, \boldsymbol{q}, t) = i\lambda f_j(|\boldsymbol{q}-\boldsymbol{k}|) e^{-i(\boldsymbol{q}-\boldsymbol{k})\cdot\boldsymbol{r}'_j(t)} e^{i\boldsymbol{q}\cdot\boldsymbol{r}''}. \tag{3}$$

$f_j(|\boldsymbol{q}-\boldsymbol{k}|)$ is the scattering factor of atom j for scattering through wave vector $\boldsymbol{q}-\boldsymbol{k}$. $\boldsymbol{r}''$ is a spatial coordinate in the detector plane, which is assumed to be in the far field.

Now we allow for non-plane-wave illumination described by a source $A(\boldsymbol{k})$, which could be complex. Summing over all the atoms and integrating over all the plane-wave components $\boldsymbol{k}$ in the illumination, we get for the total scattered wave function

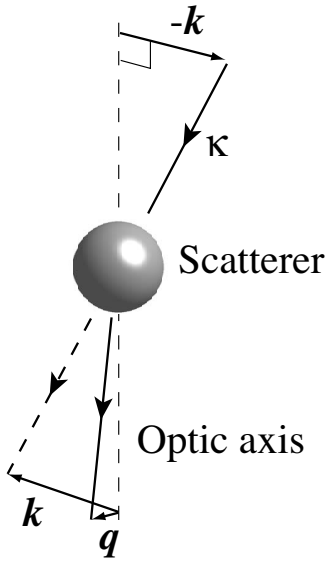

FIG. 1. Diagram showing the sample scattering geometry in its simplest form.

$$\phi(\boldsymbol{r}'', \boldsymbol{q}, t) = i\lambda e^{i\boldsymbol{q}\cdot\boldsymbol{r}''} \sum_{j=1}^{N} e^{-i\boldsymbol{q}\cdot\boldsymbol{r}'_j(t)} \int A(\boldsymbol{k}) f_j(|\boldsymbol{q}-\boldsymbol{k}|) e^{i\boldsymbol{k}\cdot\boldsymbol{r}'_j(t)} d^2\boldsymbol{k}$$
$$\approx i\lambda e^{i\boldsymbol{q}\cdot\boldsymbol{r}''} \sum_{j=1}^{N} f_j(|\boldsymbol{q}|) e^{-i\boldsymbol{q}\cdot\boldsymbol{r}'_j(t)} \int A(\boldsymbol{k}) e^{i\boldsymbol{k}\cdot\boldsymbol{r}'_j(t)} d^2\boldsymbol{k}, \tag{4}$$

where $A(\boldsymbol{k})$ is the amplitude of the incident plane wave with wave vector $\boldsymbol{k}$. In this last equation, we have used the Taylor series $f_j(|\boldsymbol{q}-\boldsymbol{k}|) \approx f_j(|\boldsymbol{q}|) - \boldsymbol{k}\cdot\nabla_q f_j(|\boldsymbol{q}|)$ and the fact that the linear gradient term across the symmetrical aperture has negligible contribution to the integral when $\boldsymbol{k}$ is small. The higher-order terms in the Taylor expansion, depending on k^2 and above, are negligible for typical aperture sizes.[22] This allows us to replace $f_j(|\boldsymbol{q}-\boldsymbol{k}|)$ inside the integral with a constant $f_j(|\boldsymbol{q}|)$ outside the integral without significant loss of accuracy. We have assumed here that the probe convergence angles are shallow and have ignored the z components of $\boldsymbol{k}$, which, being very small, introduce long-wavelength oscillatory coherence terms along z.[21] This assumption is valid if the object radius R_c is much smaller than this wavelength, that is $R_c \ll 4\pi^2/(\lambda K^2)$, where K is a measure of the range of $\boldsymbol{k}$ over which the integral is summed (i.e., the aperture radius).

The scattered intensity at time t [object location $\boldsymbol{R}(t)$] is given by $I(\boldsymbol{q}, t) = |\phi(\boldsymbol{r}'', \boldsymbol{q}, t)|^2$ to give

$$I(\boldsymbol{q}, t) = \lambda^2 \sum_{m=1}^{N} \sum_{n=1}^{N} f_m(|\boldsymbol{q}|) f_n(|\boldsymbol{q}|) e^{i\boldsymbol{q}\cdot\boldsymbol{r}_{mn}(t)} P_{mn}(K, t), \tag{5}$$

where we have set $\boldsymbol{r}_{mn} = \boldsymbol{r}_n - \boldsymbol{r}_m$. The impulse function $P_{mn}(K, t)$ is

$$P_{mn}(K, t) = \int A(\boldsymbol{k}) e^{i\boldsymbol{k}\cdot\boldsymbol{r}'_m(t)} d^2\boldsymbol{k} \int A(\boldsymbol{k}') e^{-i\boldsymbol{k}'\cdot\boldsymbol{r}'_n(t)} d^2\boldsymbol{k}'. \tag{6}$$

$P_{mn}(K, t) = 1$ for plane-wave illumination and is dimensionless. A similar expression for x-ray scattering can be ob-

tained by multiplying Eq. (6) by a polarization correction factor $(\eta+\cos^2\theta)/(\eta+1)$, where $\theta=2\sin^{-1}(\lambda q/4\pi)$ is the scattering angle. For plane-polarized x rays, $\eta=\tan\alpha$, where α is the angle between the plane of polarization of the incident x-ray beam and the plane containing both the incident and scattered beams. For circularly polarized x rays, $\eta=1$.

We now model the intensity of the illuminated region by a Gaussian, with a standard deviation for the falloff in intensity (in real space) being σ. For unit total intensity in the probe, the two-dimensional wave *amplitude* profile in k space for such a focused beam is

$$A'(\boldsymbol{k}) = \frac{\sigma}{2^{1/2}\pi^{3/2}}\exp(-\sigma^2k^2), \tag{7}$$

where $\boldsymbol{k}\equiv(k_x,k_y)$ and $k\equiv|\boldsymbol{k}|=\sqrt{(k_x^2+k_y^2)}$. $A'(\boldsymbol{k})$ is related to $A(\boldsymbol{k})$ via $A(\boldsymbol{k})=2\pi\sigma^2A'(\boldsymbol{k})$, since the Gaussian probe defined by $A(\boldsymbol{k})$ has unit intensity on the axis.

For a probe that is out of focus by a distance Δf, $A'(\boldsymbol{k})$ is modified to

$$\begin{aligned} A'(\boldsymbol{k}) &= \frac{\sigma}{2^{1/2}\pi^{3/2}}\exp(-\sigma^2k^2)\exp\left(i\frac{\lambda\Delta f}{4\pi}k^2\right) \\ &= \frac{\sigma}{2^{1/2}\pi^{3/2}}\exp\left[-\left(\sigma^2-i\frac{\lambda\Delta f}{4\pi}\right)k^2\right]. \end{aligned} \tag{8}$$

This is equivalent to a Gaussian also, with a complex standard deviation σ' given by

$$\sigma'^2 \equiv \sigma^2 - i\frac{\lambda\Delta f}{4\pi}. \tag{9}$$

We are ignoring higher-order aberration terms in this treatment. For example, spherical aberration C_s would introduce additional phase-shift terms $\exp[i(C_s\lambda^3/32\pi^3)k^4]$ and the probe would no longer be pure Gaussian, complicating the analysis.

Fourier transforming, the intensity-normalized probe wave function in real space is

$$\psi'(r,\Delta f) = \frac{\sigma}{\sqrt{2\pi}\sigma'^2}\exp\left[-\frac{r^2}{4\sigma'^2}\right], \tag{10}$$

and the probe intensity is

$$I'(\boldsymbol{r},\Delta f) = \frac{1}{2\pi}\frac{1}{\left(\sigma^2+\dfrac{\lambda^2\Delta f^2}{16\pi^2\sigma^2}\right)}\exp\left[-\frac{r^2}{2\left(\sigma^2+\dfrac{\lambda^2\Delta f^2}{16\pi^2\sigma^2}\right)}\right]. \tag{11}$$

Thus, the intensity profile of a defocused Gaussian is just another broader Gaussian with standard deviation σ_d, which is related to σ and Δf by

$$\sigma_d^2 = \sigma^2 + \frac{\lambda^2\Delta f^2}{16\pi^2\sigma^2}. \tag{12}$$

The phase shift $\varphi(r,\Delta f)$ of the defocused Gaussian probe (relative to a propagated plane wave of the same wavelength λ) is given by

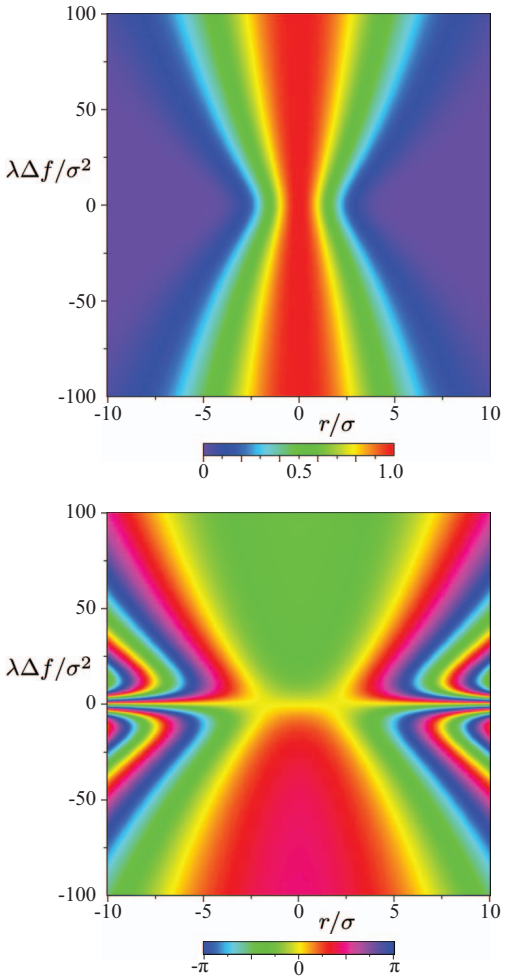

FIG. 2. (Color) Probe amplitude (top) and phase (bottom) of a Gaussian beam as a function of reduced axial radius r/σ (horizontal axis) and reduced defocus $\lambda\Delta f/\sigma^2$ (vertical axis). σ is the standard deviation of the Gaussian intensity at focus $\Delta f=0$.

$$\varphi(r,\Delta f) = \tan^{-1}\left(\frac{\lambda\Delta f}{4\pi\sigma^2}\right) - \frac{\dfrac{1}{4}\left(\dfrac{\lambda\Delta f}{4\pi\sigma^2}\right)\left(\dfrac{r}{\sigma}\right)^2}{1+\left(\dfrac{\lambda\Delta f}{4\pi\sigma^2}\right)^2}. \tag{13}$$

The first term is independent of r. The second term is parabolic in r and represents the phase retardation (when $\Delta f>0$) arising from the curvature of the diverging wave front relative to the focal plane. Recall, $\Delta f>0$ represents an overfocused probe and so the illumination at the sample is from a real Gaussian source. Conversely, $\Delta f<0$ represents an underfocused probe, where the illumination at the sample is converging toward a virtual Gaussian source. Consequently, the phase shifts are of opposite sign on either side of the focal plane $\Delta f=0$.

The dependences of the amplitude and phase of a defocused Gaussian wave on r and Δf are shown in Fig. 2. The phase is constant across the probe when in focus $\Delta f=0$. Far from focus, the phase on axis at $r=0$ shifts by $\pm\pi/2$, with the same sign as Δf.

To model linear motion of a rigid nonrotating cluster, we rewrite Eq. (1) as

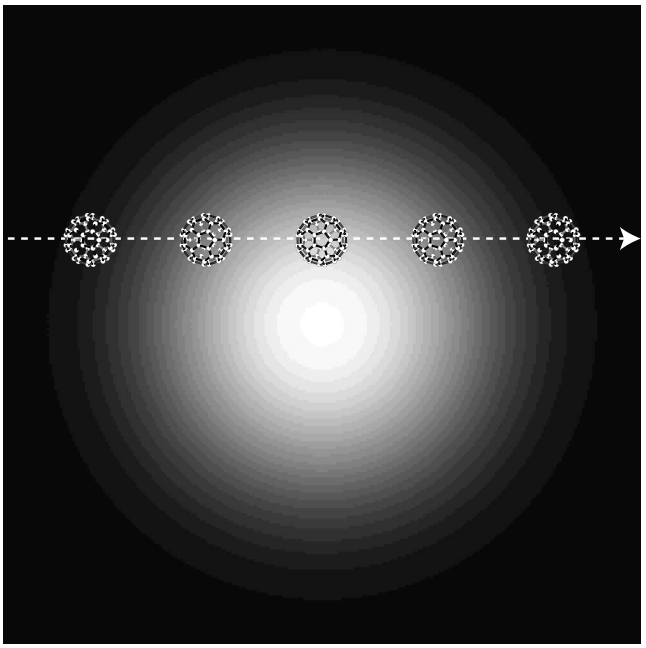

FIG. 3. Illustration of a C_{60} molecule in various locations as it transits a Gaussian beam. Phase and amplitude gradients across the molecule affect the diffracted intensities.

$$\boldsymbol{r}_j'(t) = \boldsymbol{v}t + \boldsymbol{R}_0 + \boldsymbol{r}_j, \tag{14}$$

where the velocity $\boldsymbol{v}$ is constant and $\boldsymbol{R}_0$ is a constant offset. It is convenient to assume that $\boldsymbol{v}$ is aligned along the x axis so $\boldsymbol{v} \equiv (v,0,0)$ (Fig. 3).

First, for a stationary scatterer ($v=0$) it is straightforward to integrate Eq. (6) with respect to time to obtain for the intensity after exposure time τ,

$$I(\boldsymbol{q}) = \frac{2\pi\sigma^4 I_0 \lambda^2 \tau}{\sigma_d^2} \sum_{m=1}^{N}\sum_{n=1}^{N} f_m(|\boldsymbol{q}|) f_n(|\boldsymbol{q}|) e^{i\boldsymbol{q}\cdot\boldsymbol{r}_{mn}} \times \exp\left[-\frac{(r_m^2 + r_n^2)}{4\sigma_d^2}\right] \exp\left[i\frac{\lambda\Delta f}{\sigma^2}\frac{(r_n^2 - r_m^2)}{4\sigma_d^2}\right]. \tag{15}$$

I_0 is the incident flux (particles per unit area per unit time). In this expression, we have merged the constant offset $\boldsymbol{R}_0$ into the r coordinates. This equation reveals oscillatory terms that depend on the difference $(r_n^2 - r_m^2)$, similar to the behavior of a zone plate. This expression can be rewritten in an alternative form

$$I(\boldsymbol{q}) = \frac{2\pi\sigma^4 I_0 \lambda^2 \tau}{\sigma_d^2} \sum_{m=1}^{N}\sum_{n=1}^{N} f_m(|\boldsymbol{q}|) f_n(|\boldsymbol{q}|) e^{i(\boldsymbol{q}+\boldsymbol{Q}_{mn})\cdot\boldsymbol{r}_{mn}} \times \exp\left[-\frac{(r_m^2 + r_n^2)}{4\sigma_d^2}\right], \tag{16}$$

where

$$\boldsymbol{Q}_{mn} = \frac{\lambda\Delta f}{4\sigma^2\sigma_d^2}(\boldsymbol{r}_m + \boldsymbol{r}_n). \tag{17}$$

$\boldsymbol{Q}_{mn}$ grows for those scatterers that are far from the geometric center and is zero when $\Delta f = 0$. Equation (16) can be interpreted as if the interference term from each atom pair m,n has its own origin in the diffraction plane $-\boldsymbol{Q}_{mn}$ caused by local tilt in the wave front. It is peculiar that although the $\boldsymbol{Q}_{mn}$ term acts as a reciprocal-lattice vector, it is in fact proportional to the real-space vector $\boldsymbol{r}_m + \boldsymbol{r}_n$. $\boldsymbol{Q}_{mn}$ differs for each atom pair because of curvature in the wave front and so does not result in a uniform sideways displacement of the whole pattern. Instead, the pattern is distorted, reflecting the symmetry of the object plus the probe wave front. $\boldsymbol{Q}_{mn}$ can be large when the cluster is far from the center of the probe and when the defocus Δf is large. Even when $\Delta f = 0$, there remains a damping term $\exp[-(r_m^2 + r_n^2)/4\sigma^2]$, which also has its strongest effect on the interference between atoms that are far from the beam axis. An inversion procedure that presumes plane-wave illumination in order to recover the object will obtain a result that contains distortions due to wave front curvature in the probe and amplitude gradients. It is important to make sure that such curvature and gradients are small if the plane-wave approximation is to be valid for the phase-retrieval algorithm.

For a scatterer moving along x [$\boldsymbol{v} = (v,0,0)$, $v \neq 0$], the time-averaged diffraction signal can be shown to be

$$I(\boldsymbol{q}) = \frac{\lambda^2\sqrt{2\pi}\sigma^2 I_0}{\sigma_d v} \sum_{m=1}^{N}\sum_{n=1}^{N} f_m(|\boldsymbol{q}|) f_n(|\boldsymbol{q}|) e^{i\boldsymbol{q}\cdot\boldsymbol{r}_{mn}} \times \exp\left[-\frac{x_{mn}^2}{8\sigma^2}\right] \exp\left[-\frac{(y_m^2 + y_n^2)}{4\sigma_d^2}\right] \times \exp\left[i\frac{\lambda\Delta f}{\sigma^2}\frac{(y_n^2 - y_m^2)}{4\sigma_d^2}\right]. \tag{18}$$

τ does not appear in this expression as we have integrated over infinite time. The time averaging affects only the x components. As v increases, the total signal drops because the molecule's dwell time under the probe is reduced in proportion to $1/v$. The signal also decreases when the probe is defocused since σ_d is enlarged. The probe is spread out over two dimensions, reducing the local intensity in proportion to $1/\sigma_d^2$, but the path length traversed by the molecule under the probe increases linearly in proportion to σ_d. These two competing effects produce the $1/\sigma_d$ dependence seen in Eq. (18). The largest damping occurs when $x_{mn} = x_n - x_m$ is large. Thus, nearest-neighbor interferences are the least affected. The biggest impact on the diffraction patterns due to time averaging therefore tends to be on the low-$\boldsymbol{q}$ vectors along x, corresponding to the largest x-component spacings between atoms.

Time-averaging appears to introduce a strong effect for the x coordinates. However, as Eqs. (15) and (16) reveal, the instantaneous diffraction patterns are also affected by the probe properties. If successive molecules diffract from different locations in the probe, differences between diffraction patterns will not be caused entirely by differences in molecule orientation. The scattering is from a system—the molecule plus the probe. It is only when each molecule scatters from the same location within a reproducible probe that the differences in diffraction can be attributed entirely to differences in molecule orientation.

III. SIMULATIONS

Electron diffraction wave functions from a C_{60} molecule were simulated using Eq. (4) for a Gaussian probe

$$\phi(\boldsymbol{q}) = \sum_{j=1}^{60} f_j(|\boldsymbol{q}|)\exp(-i\boldsymbol{q}\cdot\boldsymbol{r}'_j)\exp(-r'^2_j/4\sigma'^2). \quad (19)$$

The scattered wave functions were calculated using a modified version of the C program VKMAP written by one of us (MMJT) for fluctuation electron microscopy simulations. The constant multiplication factors were omitted here since it is only the relative intensities that are important. Curvature of the Ewald sphere was included by assigning a sagittal z component to the scattering wave vector, $q_z=(\lambda/4\pi)q^2$, which is valid provided $q \ll 4\pi/\lambda$. λ is the electron wavelength, which was set at $\lambda=3.7$ pm (i.e., 100 kV electrons), and q is the scattering vector component in the $x-y$ plane. σ'^2 is given by Eq. (9). The C_{60} molecule was oriented so that one of the $\bar{5}$ axes was parallel to the illumination direction, z [Figs. 3 and 5(j)]. The molecule was translated rigidly, without rotation, across the probe along the x axis from $x=-5\sigma_d$ to $x=+5\sigma_d$ in 99 steps, with step number 50 having the molecule centered on the illumination axis. At each location, the diffracted intensity $I(\boldsymbol{q})=\phi^*(\boldsymbol{q})\phi(\boldsymbol{q})$ was stored out to wave vectors of $-5.12\ \text{nm}^{-1} \le q_x/2\pi,\ q_y/2\pi \le 5.12\ \text{nm}^{-1}$. Each pattern was sampled into a 512×512 array, with $q=0$ centered at pixel location (256, 256).

The simulated diffraction data were then inverted using a charge-flipping algorithm,[16,17] following the method described by Wu *et al.*[15] This method was chosen for its simplicity and ease of implementation. The approaches by Fienup,[14] Rodenburg and co-workers,[10–12] and Quiney *et al.*[13] may offer more robust methods when wave curvature is present. In our implementation of charge flipping, the "observed" diffraction amplitudes $F^{\text{obs}}(\boldsymbol{q})$ are the 512×512 values obtained by taking $F^{\text{obs}}(\boldsymbol{q})=\sqrt{I(\boldsymbol{q})}$. The algorithm was implemented in a DIGITALMICROGRAPH™ script on a Macintosh™ computer. Our implementation differed from that of Wu *et al.*[15] in that we allowed the charge-flipping threshold to decrease from 0.15 to 0.01 as the run progressed. Usually, but not always, this allowed a more stable convergence for our simulated data. We also experimented with a hybrid input-output (HIO) method, as advocated by Wu *et al.*,[15] but our implementation did not improve convergence rates. The inversion was accomplished by repeatedly running the charge-flipping code under different starting conditions and keeping the best result. Generally, the runs were seeded with a random object and the charge-flipping threshold set to 0.15, although sometimes smaller values as low as 0.01 appeared to work better. The convergence was followed by examining the residual at the kth charge flip step

$$R^k = \frac{\sum_{\boldsymbol{q}} ||F^k(\boldsymbol{q})| - |F^{\text{obs}}(\boldsymbol{q})||}{\sum_{\boldsymbol{q}} |F^{\text{obs}}(\boldsymbol{q})|}. \quad (20)$$

Each run usually rendered the lowest residual after about 40 charge flips, after which the residual would increase. Subsequent runs were seeded by the best previous result, and the charge-flipping threshold would sometimes be lowered further. In total, between 200 to 10 000 charge-flipping steps were required to achieve a stable final result whose R value could not be lowered further within a reasonable time.

The charge-flipping inversion method used here employed standard fast Fourier transforms (FFTs). The use of FFTs is equivalent to treating the scatterer as a simple projection of a phase object, ignoring curvature in the Ewald sphere. Since our diffraction simulations incorporated the Ewald sphere, our best R values were never less than 0.25.

Shot noise was introduced into diffraction patterns by the following procedure. First the noise-free pattern was computed as a two-dimensional array pattern measuring x dim by y dim pixels. Then a linear array *accum* was constructed, with the same number of elements as the number of pixels in the two-dimensional array pattern x dim $\times$ y dim. Beginning with the first pattern pixel, which is *pattern*(0,0) in a zero-based array, *accum* stores the accumulated intensity as we scan along each row. Thus, the linear array element *accum*($x$dim$\times j+i$) contains the sum of all the pattern pixels between *pattern*(0,0) and *pattern*(i,j), where we have scanned successively along each row j in *pattern*. The final element *accum*($x$dim$\times y$dim-1) contains the total intensity in *pattern*. The array *accum* is then normalized by dividing throughout by this total intensity so that its values range from approximately $\gtrsim$0.0 at the beginning to approximately $\lesssim$1.0 at the end. A new two-dimensional array, *noisypattern* of $x$dim$\times y$dim pixels, is created and initialized to zero everywhere, which will contain the noisy diffraction pattern. A random number between 0 and 1 is generated, and the entry *accum*(n) with the closest value to the random number is found. Since the values in *accum* are already sorted, the closest value can be found efficiently in $O[\ln(x\ \text{dim}\times y\ \text{dim})]$ steps (in our case, for $x$dim$=y$dim$=512$, this is $\sim$12 steps) by recursively bracketing and halving the range of possible values within *accum*. One count is added to the noisy pattern at pixel *noisypattern*($n\%\ x$dim,n/xdim), where "/" represents integer division, rounding down to the nearest integer (giving the row number), and "%" represents the remainder of the integer division (giving the column number). To generate a diffraction pattern with a total of N counts, this procedure is repeated with N random numbers, accumulating one count each time at the appropriate pixel. This method correctly weights the randomized accumulation of counts toward the more intense peaks and reproduces the original diffraction pattern accurately when N is large, $N>10^6$ in our case. We used Knuth's random number procedure RAN3 as provided in Ref. 23.

IV. RESULTS AND DISCUSSION

Diffraction patterns were simulated for a C_{60} molecule using a Gaussian-profile electron probe, with standard deviation $\sigma=0.25$ nm. In the first set of simulations, the probe was focused $\Delta f=0$. Two of the 99 diffraction patterns are shown in the top row of Figs. 4(a) and 4(b) when the center of the C_{60} molecule was located at $x=0$ and $x=+2.5\sigma$ (i.e., at $x=0$ and 0.625 nm, respectively). The time-averaged dif-

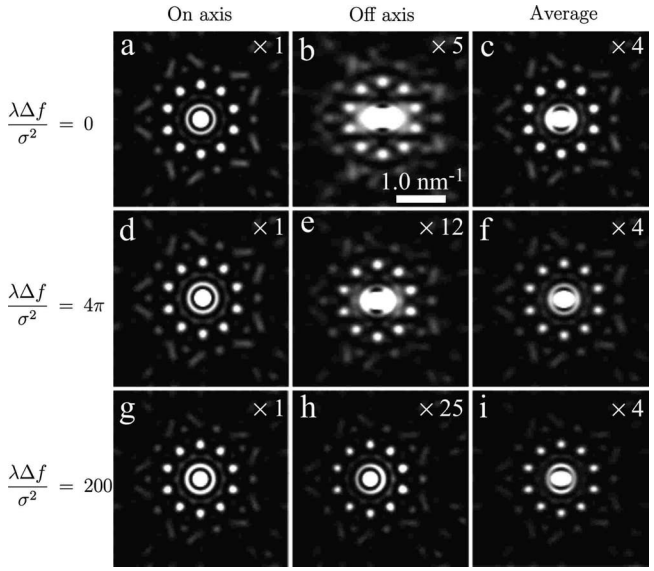

FIG. 4. Diffraction patterns calculated for a C_{60} molecule, viewed down a $\bar{5}$ axis, for a Gaussian probe profile with $\sigma = 0.25$ nm. The three rows are for the three normalized defocus values $\lambda\Delta f/\sigma^2 = 0$, 4π, and 200, respectively. The left column is for the case when the center of the molecule is on axis, the central column for when the molecule is at $x = 2.5\sigma_d$ for (b) and (e), and $x = 5.0\sigma_d$ for (h). The third column is the time-averaged pattern for the molecule's transit across the center of the probe. The linear intensity scaling factor relative to the centered pattern in the left column of each row is indicated in the upper right of each pattern.

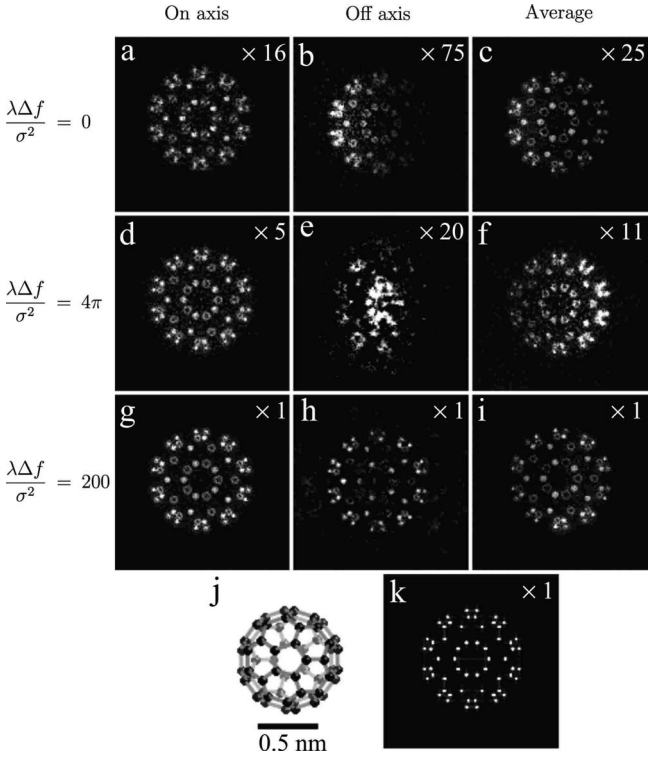

FIG. 5. (a)–(i) are reconstructions of the C_{60} molecule using the charge-flipping algorithm for Gaussian illumination with $\sigma = 0.25$ nm. Each panel represents a reconstruction of the corresponding diffraction pattern in Fig. 4. (j) C_{60} molecule, viewed down the $\bar{5}$ axis, that was used for the diffraction simulations. (k) Projected charge density of the C_{60} molecule. All intensity scales are linear. The intensity multiplication factors applied to each reconstruction, to allow visual comparison to the best reconstruction shown in (g), are indicated in the upper right of each figure.

fraction pattern is shown at the end of the row [Fig. 4(c)]. The nominal projected width of a C_{60} molecule is ~0.71 nm, atom center to center. The diffraction patterns at $x = \pm 2.5\sigma$ are identical, and we show only the pattern at $x = +2.5\sigma$ [Fig. 4(b)]. They are significantly different to the centered pattern [Fig. 4(a)]. The high $\boldsymbol{q}$ information is suppressed, and the low $\boldsymbol{q}$ data are broadened along the motion direction x. There are no phase gradients across the focused Gaussian probe. These diffraction effects are caused by the amplitude gradient in the probe. The time-averaged diffraction pattern for the molecule traversing the probe [Fig. 4(c)] closely resembles the pattern at $x = 0$. The most significant difference is that the low $\boldsymbol{q}$ data are broadened. The patterns at larger x are weaker in overall intensity, and the averaged pattern is dominated by the highest-intensity data obtained close to $x = 0$. The intensity scaling factors relative to the centered patterns in the left column are indicated in the upper right corner of each pattern.

Diffraction patterns were also simulated for a defocused probe, again with $\sigma = 0.25$ nm, but with $\lambda\Delta f/\sigma^2 = 4\pi$ (i.e., $\Delta f = 212.3$ nm for 3.7 pm wavelength electrons). At this defocus, $\sigma_d = 0.354$ nm [Eq. (12)]. Two patterns taken at $x = 0$ and $x = +2.5\sigma_d$ are shown in the second row of Figs. 4(d) and 4(e), with the time-averaged pattern presented at the end of the row [Fig. 4(f)].

A similar series of patterns was computed for a more strongly defocused probe, with $\sigma = 0.25$ nm and $\lambda\Delta f/\sigma^2 = 200$ (i.e., $\Delta f = 3378$ nm for 3.7 pm wavelength electrons). At this defocus, $\sigma_d = 3.99$ nm. Two patterns taken at $x = 0$ and $x = +5\sigma_d$ are shown in the third row of Fig. 4. Because the probe is strongly defocused (i.e., $\lambda\Delta f/\sigma^2 \gg 4\pi$), causing the illuminated region to resemble a spherical wave, the patterns are all quite similar, except that the pattern at $x = 5\sigma_d$ [Fig. 4(h)] is about a factor of 25 weaker in intensity. The origin of each pattern moves as the C_{60} molecule transits the probe. This is a direct consequence of the $\boldsymbol{Q}_{mn}$ terms [Eqs. (16) and (17)] which are no longer zero when the probe is defocused and when the object center is off the probe axis. The shift is also apparent between Figs. 4(d) and 4(e), but is more pronounced at the larger defocus [between Figs. 4(g) and 4(h)]. Since $x > 0$, the shift is to the left in the $-q_x$ direction in these simulations. This origin shift can also be understood by noting that the average direction of the spherical wave front changes as the object moves across the probe. Consequently, for a defocused probe, it is the phase shifts that distort the average diffraction pattern most, and the impact is greatest for the low $\boldsymbol{q}$ scattering vectors. With care, these origin shifts could probably be detected and measured in experimental data, allowing simulations to correct for them.

The structure of the C_{60} molecule is shown in Fig. 5(j). The view is along one of the $\bar{5}$ axes, which is z in our coordinate system. x is horizontal and y is vertical in the figure. To test our algorithms, the diffraction amplitude and phase

were computed for plane-wave illumination and then inverse Fourier transformed to obtain a charge density. Figure 5(k) shows the projected charge density when the Ewald sphere was treated as having infinite radius ($\lambda \to 0$). For this flat Ewald sphere, the charge density matches the model well. For the curved Ewald sphere used in our simulations, the effective charge density closely resembles that in Fig. 5(k), but is not identical.

Reconstructions of the C_{60} molecule, obtained by applying the charge-flipping algorithm to the diffraction data of Fig. 4, are presented in Fig. 5. Reconstructions for the focused probe when $x=0$, $x=+2.5\sigma$ (where $\sigma=0.25$ nm), and for the time-averaged pattern are shown in Figs. 5(a)–5(c), respectively. The reconstruction for the on-axis molecule position [Fig. 5(a)] is respectable, with atom positions essentially resolved. However, there is significant residual charge density located between the projected atom positions. The image intensity needed to be scaled by 16 times to match the intensity scale of the projected potential [Fig. 5(k)]. The intensity gradient in the reconstruction in Fig. 5(b) arises because of the overall wave amplitude gradient across the molecule that arises when it is not coaxial with the probe. We found two equally stable results for the case of Fig. 5(b), which were left-right mirror images of each other: reconstructions related by inversion symmetry are equally viable solutions under the plane-wave approximation when $x \neq 0$.

Reconstructions for the defocus condition $\lambda \Delta f/\sigma^2=4\pi$ are presented in the next row [Figs. 5(d)–5(f)]. This is the condition that enlarges the probe width by $\sqrt{2}$ and introduces strong phase gradients (see Fig. 2). Again, the best reconstruction of the object occurs for $x=0$ [Fig. 5(d)]. The charge-flipping reconstruction distinguishes between those atoms (regions of high charge density) in the upper ($z_j>0$) and those in the lower ($z_j<0$) hemispheres of the molecule. In our simulations, atoms in the upper hemisphere appear as hollow regions of charge density. Information about the $\bar{5}$ axis, as opposed to the projected tenfold axis observed in the diffraction intensities close to the origin, comes from the higher-order Laue zones. When the molecule is off axis [Fig. 5(e)], the reconstruction is poor. Our best time-averaged reconstruction [Fig. 5(f)] does not show inversion symmetry, with more charge appearing on the right side (or on the left side with equal probability). This indicates that our charge-flipping method cannot reconcile the low-q and the high-q information, which are altered differently by the averaging.

Reconstructions for the stronger defocus condition $\lambda \Delta f/\sigma^2=200$, $\sigma_d=3.99$ nm are shown in the bottom row [Figs. 5(g)–5(i)]. The best reconstruction in this tableau occurs for $x=0$ [Fig. 5(g)], where every atom is resolved and atoms in the upper and lower hemispheres are distinguishable by whether or not they are hollow. The reconstruction at $x=5\sigma_d$ [Fig. 5(i)] is poor, although the reconstruction at $x=2.5\sigma_d$ (not shown) was comparable to that in Fig. 5(g). The time-averaged reconstruction also shows subtle departures from inversion symmetry [Fig. 5(i)].

Not apparent in these reconstructions is the relative ease with which they were obtained. Our best result, for $x=0$, $\lambda \Delta f/\sigma^2=200$ [Fig. 5(g)], required only 200 charge-inversion steps starting from a random object. Other reconstructions at $x=0$ required approximately 500 charge inversions. The reconstruction for $x=2.5\sigma_d$, $\lambda \Delta f/\sigma^2=4\pi$ [Fig. 5(e)] required 10 000 steps and could not be cajoled into a more symmetric result. The residuals for all of the best reconstructions were $R \approx 0.3$. Notably, for the best result shown in Fig. 5(g), $R=0.26$. We suspect that this can never be made zero in our reconstruction method because our diffraction simulations incorporate the Ewald sphere curvature, whereas the charge-flipping algorithm presumes a flat Ewald sphere. Reconstructions from off-axis patterns converged much more slowly than the on-axis results. Reconstructions obtained off axis and for the time-averaged diffraction data are noisy compared to the reconstruction for the on-axis condition.

Shot noise is clearly going to affect the reconstructions adversely. To explore this, we simulated shot noise by randomly filling an array with N counts, weighted appropriately by the computed noise-free diffraction pattern, as described in Sec. III. We chose the on-axis condition $\lambda \Delta f/\sigma^2=200$, since this produced our best reconstruction in the noise-free simulations [Fig. 5(g)]. We attempted reconstructions for $N=10^5$, 10^4, and 10^3 counts over the full diffraction range ($q_x/2\pi=\pm 5.12$ nm^{-1}, $q_y/2\pi=\pm 5.12$ nm^{-1}). These counts refer to scattered electrons and exclude the unscattered beam. We assumed that the detector has a 100% detection efficiency and ignored electronic noise such as dark currents, etc. In addition to the shot noise, there is an additional binning noise that is unavoidable, which is related to the fact that we rounded our random numbers to the nearest value in the computed diffraction pattern. This noise is related to the so-called "quantization noise" introduced by the finite number of binning levels in charge coupled device (CCD) detectors.

For a total count of 10^5 electrons, the reconstruction is already significantly degraded [Figs. 6(a) and 6(b)]. The R value for the reconstruction in Fig. 6(b) is $R=1.46$. However, the individual atoms are still resolvable. For $N=10^4$ counts, the diffraction pattern is visibly degraded and the reconstruction exhibits approximate fivefold symmetry. Here, $R=3.14$ and individual atoms are no longer resolved [Figs. 6(c) and 6(d)]. When $N=10^3$ counts, the reconstruction fails to resolve any significant internal details of the molecule, $R=8.95$ [Figs. 6(e) and 6(f)]. Clearly, noise in the diffraction patterns is an important limiting factor in reconstructions. Reconstructions that were marginal in the noise-free limit, such as those shown in Figs. 5(b), 5(f), and 5(h), will be vulnerable to even small amounts of noise. Signal can be improved by focusing the beam, but this comes at the expense of increasing the beam curvature.

For accurate reconstructions of the object, in addition to high signal-to-noise ratio, we need spatially coherent illumination with coherence width larger than the characteristic object width $2R_c$. The focused Gaussian probe has no phase gradients, but does have amplitude gradients. Our model of a Gaussian probe shows that defocusing the illumination reduces the wave amplitude gradients near the axis, but introduces phase gradients (Fig. 2). For the plane-wave approximation to be valid, the wave curvature across the object should be such that there is much less than a $\pi/2$ phase change between the center and the edge. From Eq. (15), we can estimate the phase difference $\Delta\varphi$ between the center and

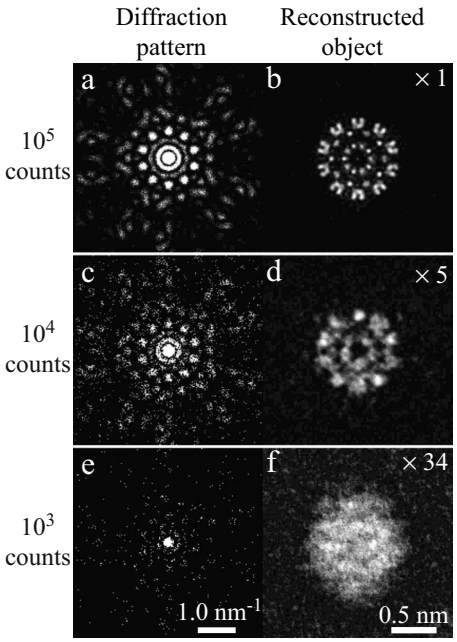

FIG. 6. Three reconstructions of a C_{60} molecule illustrating the impact of noise. The left column shows diffraction patterns for a C_{60} molecule that is centered on the illumination with $\lambda\Delta f/\sigma^2=200$. These are similar to the conditions used for Figs. 4(g) and 5(g), except those were noise free. The diffraction patterns contain a total of 10^5, 10^4, and 10^3 scattering counts within the collection range (± 5.12 nm^{-1}, ± 5.12 nm^{-1}). The detector is assumed to have a 100% detection efficiency, and the unscattered beam is not included in the count. The right column shows the corresponding reconstruction of the C_{60} molecule. Our reconstruction for 10^3 counts in (f) did not resolve any internal structural details of the C_{60} molecule. The intensity rescaling for each reconstruction is indicated in the upper right of (b), (d), and (f).

the outer radius R_c of the cluster, where $r_n^2-r_m^2=R_c^2$ to be

$$\Delta\varphi=\frac{\Delta}{1+(\Delta/4\pi)^2}\frac{R_c^2}{4\sigma^2}, \tag{21}$$

where we have set $\Delta=\lambda\Delta f/\sigma^2$. The phase difference is zero when $\Delta=0$ and $\Delta\to\infty$. It is maximum when $\Delta=4\pi$. For $\Delta\varphi\ll\pi/2$, we then need $R_c\ll\sigma$ at this defocus condition. If we demand that the phase difference across the molecule must not exceed some value $\Delta\varphi_c$ for successful phase retrieval, then we obtain the constraint $\sigma\sigma_d\geq\pi R_c^2/\Delta\varphi_c$. Setting $\Delta\varphi_c=\pi/4$, this constraint becomes $\sqrt{\sigma\sigma_d}\geq 2R_c$. In addition, Eq. (15) shows that there is a Gaussian falloff in intensity between the center and the edge. If we set $R_c=\sigma$, then the interference terms between the center and the edge are additionally attenuated by a factor $\exp(-1/8)\approx 0.88$, which is significant. To minimize phase gradients, we need either σ to be large, where the probe can be focused ($\Delta=0$), or if σ is small, Δ needs to be large. In our simulations, the object recovery was poor under focused-probe conditions. To avoid amplitude gradient effects, we used an enlarged probe obtained by defocusing [Eq. (12)] setting $\Delta=\lambda\Delta f/\sigma^2=200>4\pi$. We could then invert the object satisfactorily, provided the object and probe were coaxial. For our simulations, we observed empirically the rule-of-thumb condition that $\sigma_d\geq 10R_c$ for success, which is generally consistent with the more formal constraint on the phase difference presented above. It would appear that in order to ensure accurate inversion, the illumination probe should be sufficiently defocused. However, there is a competing requirement—that of maintaining a sufficiently high intensity at the scatterer in order to improve the signal-to-noise ratio. The scattering from a single molecule is weak, and broadening the beam by defocusing it reduces the signal in proportion to $1/\sigma_d$ for the time-averaged signal or $1/\sigma_d^2$ for the instantaneous signal. In practice, focused probes have the advantage of increasing the signal, but at the possible disadvantage of introducing amplitude and phase gradients.

For three-dimensional reconstruction of molecules, diffraction patterns from many orientations of similar objects are needed. It has been proposed that molecular structures can be determined by using intense femtosecond-duration pulses in "diffract-and-destroy" experiments.[1,4,7] Such fast probes acquire a molecular snapshot, the precise details of the diffraction pattern depending on the instantaneous molecule orientation and location within the pulse. The diffraction pattern will have an origin shift and a distortion caused by the $\boldsymbol{Q}_{mn}$ terms [Eqs. (16) and (17)]. The origin shift may provide a simple way of locating the object within the probe. Additionally, diffraction intensities are modified by the amplitude gradient terms. If the diffraction data from a large number of identical molecules are not all from the same location within the probe, there will be additional uncontrolled position parameters to solve in the reconstruction.

Defocused Gaussian probes are perhaps the most benign type of probe for phase-retrieval experiments. Focusing lenses have aberrations, such as spherical aberration and coma, which tend to increase local wave front curvature in probes. We would expect phase gradients to be stronger in real probes, compared to those modeled here, unless the sources are strongly defocused.

The arguments presented here can be applied to probes formed by pinholes, where the $A(\boldsymbol{k})$ functions represent defocused Airy disks. The above criteria applied to this case show that the pinhole diameter should be much larger than the object diameter. Again, this comes at the expense of reduced signal compared to the unscattered beam.

Although we developed our model for kinematical electron scattering, our method is readily extended to kinematical x ray and neutron scattering. For x rays, a polarization factor must be included. Expressed in terms of the dimensionless parameters $\lambda\Delta f/\sigma_d^2$ and $\boldsymbol{r}/\sigma_d$, the different length scales can be accommodated.

In the analysis conducted here, we used a simple charge-flipping algorithm based on the phase-object approximation. This approximation is not a fundamental limitation of the algorithm, and recently developed phase-retrieval techniques that incorporate knowledge of the actual probe profile should offer significant improvement.[10–14]

The issues discussed here are also of direct relevance to the technique of fluctuation microscopy.[21,24] Speckle statistics of the scattering in disordered samples are affected by the coherence of the illumination. Normally, fluctuation microscopy experiments are conducted at the focused condi-

tion. The detailed behavior of the sample speckle as a function of probe focus has not yet been fully explored.[25,26] However, it is clear from our analysis (summarized in Fig. 2) that the coherence width of a defocused Gaussian beam broadens more slowly than the beam width itself. This suggests that defocus is not an effective method for changing the effective coherence width of the probe in fluctuation microscopy experiments.

V. CONCLUSION

We have presented a simple kinematical scattering model for the diffraction from a molecule that is irradiated by a concentrated illumination probe. We have explored the model case where a Gaussian intensity profile electron beam probes a C_{60} molecule. A plane-wave scattering model shows that the longest interatomic distances within the molecule are affected most by the distortions induced by wave front curvature and amplitude gradients. The nearest-neighbor information is affected least. Diffraction simulations from a C_{60} molecule, under various conditions of defocus, were inverted using a charge-flipping algorithm (assuming plane-wave illumination) to recover the projected charge density of the object. We find that the object can be recovered satisfactorily in the plane-wave approximation when it is centered on the probe, provided that the intensity standard deviation $\sigma_d \geq 10R_c$, where R_c is the nominal radius of the cluster. Empirically, the value of $\sigma_d \sim 10R_c$ appears to be about optimum for our simulations using the plane-wave approximation and the charge-flipping object-recovery algorithm. A larger value of σ_d improves the plane-wave assumption, but the amount of signal that is "wasted" also increases. The quality of the recovered object deteriorates when it is not centered on the illumination or if the illumination is too finely focused. In addition, the time-averaged diffraction pattern, acquired as the object moves across the illuminated region (even if it is rigid and not rotating), results in poor object recovery. The plane-wave approximation improves when the illumination is further out of focus, but this comes at the expense of reduced signal. Object recovery is also sensitive to the presence of shot noise. For our reconstruction of a C_{60} molecule, we found that a total scattering signal of over 10^5 counts in the range $|q_x/2\pi|, |q_y/2\pi| \leq 5.12$ nm^{-1} is desirable. However, more sophisticated information-optimizing recovery methods (similar to the maximum-entropy and Richardson-Lucy algorithms, which were not explored here) may improve the tolerance to noise.

Ideally, for diffract-and-destroy experiments using focused pulsed illumination on a beam of identical molecules, the phase-retrieval algorithm should solve for the object plus the probe wave function under conditions of high signal-to-noise ratio. The positional degrees of freedom in the phase retrieval can be reduced significantly if all diffraction patterns are from the same molecule location within the probe.

ACKNOWLEDGMENTS

We are grateful to L. Fan, D. Kumar, and I. McNulty for fruitful discussions, and we thank the Office of Science, Office of Basic Energy Sciences, U.S. Department of Energy for support to the Advanced Photon Source through Contract No. DE-AC02-06CH11357.

[1] R. Neutze, R. Wouts, D. van der Spoel, E. Weckert, and J. Hajdu, Nature (London) **406**, 752 (2000).
[2] J. C. H. Spence and R. B. Doak, Phys. Rev. Lett. **92**, 198102 (2004).
[3] H. N. Chapman *et al.*, J. Opt. Soc. Am. A **23**, 1179 (2006).
[4] H. N. Chapman *et al.*, Nat. Phys. **2**, 839 (2006).
[5] S. Marchesini *et al.*, Opt. Express **11**, 2344 (2003).
[6] D. A. Shapiro *et al.*, J. Synchrotron Radiat. **15**, 593 (2008).
[7] J. C. H. Spence, Nat. Photonics **2**, 390 (2008).
[8] R. M. Glaeser, K. Downing, D. DeRosier, W. Chiu, and J. Frank, *Electron Crystallography of Biological Macromolecules* (Oxford University Press, Oxford, UK, 2007).
[9] U. Weierstall, R. B. Doak, J. C. H. Spence, D. Starodub, D. Shapiro, P. Kennedy, J. Warner, G. G. Hembree, P. Fromme, and H. N. Chapman, Exp. Fluids **44**, 675 (2008)
[10] J. M. Rodenburg and H. M. L. Faulkner, Appl. Phys. Lett. **85**, 4795 (2004).
[11] J. Rodenburg, A. Hurst, and A. Cullis, Ultramicroscopy **107**, 227 (2007).
[12] J. M. Rodenburg, A. C. Hurst, A. G. Cullis, B. R. Dobson, F. Pfeiffer, O. Bunk, C. David, K. Jefimovs, and I. Johnson, Phys. Rev. Lett. **98**, 034801 (2007).
[13] H. M. Quiney, G. J. Williams, and K. A. Nugent, Opt. Express **16**, 6896 (2008).
[14] J. R. Fienup, Appl. Opt. **21**, 2758 (1982).
[15] J. Wu, K. Leinenweber, J. C. H. Spence, and M. O'Keeffe, Nature Mater. **5**, 647 (2006).
[16] G. Oszlányi and A. Süto, Acta Crystallogr., Sect. A: Found. Crystallogr. **60**, 134 (2004).
[17] G. Oszlányi and A. Süto, Acta Crystallogr., Sect. A: Found. Crystallogr. **61**, 147 (2005).
[18] For x rays, it is the ionization response time that is important since the scattering is mostly from the electrons.
[19] M. M. J. Treacy and J. M. Gibson, Ultramicroscopy **52**, 31 (1993).
[20] M. M. J. Treacy and J. M. Gibson, Ultramicroscopy **54**, 93 (1994).
[21] M. M. J. Treacy and J. M. Gibson, Acta Crystallogr., Sect. A: Found. Crystallogr. **52**, 212 (1996).
[22] M. M. J. Treacy and J. M. Gibson, J. Microsc. **180**, 2 (1995).
[23] W. H. Press, S. A. Teukolsky, W. T. Vetterling, and B. P. Flannery, *Numerical Recipes in C: The Art of Scientific Computing*, 2nd ed. (Cambridge University Press, Cambridge, 1992).
[24] M. M. J. Treacy, Microscopy Today **13**, 20 (2005).
[25] J. M. Cowley, Ultramicroscopy **90**, 197 (2002).
[26] L. Fan, I. McNulty, D. J. Paterson, M. M. J. Treacy, and J. M. Gibson, *Neutron and X-ray Scattering as Probes of Multiscale Phenomena*, MRS Symposia Proceedings No. 840 (Materials Research Society, Pittsburgh, 2005), p. Q6.7.1.